Enhanced nanoscale conduction capability of a MoO$_2$/Graphene composite for high performance anodes in lithium ion batteries

Akkisetty Bhaskar [a], Melepurath Deepa [a,*], T.N. Rao [b], U.V. Varadaraju [c]

[a] *Indian Institute of Technology Hyderabad, Ordnance Factory Estate, Yeddumailaram 502205, Andhra Pradesh, India*
[b] *Center for Nanomaterials, ARCI, Hyderabad 500005, India*
[c] *Department of Chemistry, Indian Institute of Technology Madras, Chennai 600036, India*

HIGHLIGHTS

► MoO$_2$/Graphene composite by a one pot low temperature *in-situ* solution reduction method.
► Uniform entrapment of MoO$_2$ nanoparticles in 2D graphene scaffolds.
► An eight order increase in nanoscale conductivity of MoO$_2$/Graphene relative to MoO$_2$.
► Unparalleled reversible capacity of 770 mAh g^{-1} at 540 mA g^{-1} for MoO$_2$/Graphene.
► A coulombic efficiency of almost 100% retained even after 1000 cycles.

GRAPHICAL ABSTRACT
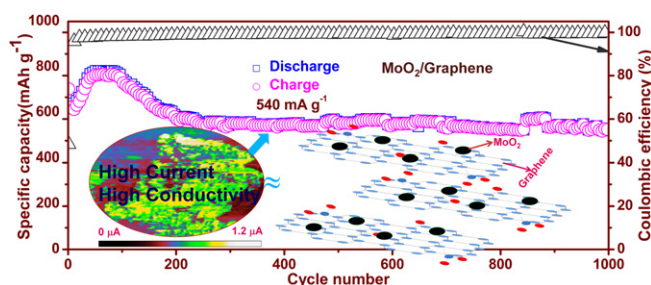
ABSTRACT

A MoO$_2$/Graphene composite as a high performance anode for Li ion batteries is synthesized by a one pot *in-situ* low temperature solution phase reduction method. Electron microscopy and Raman spectroscopy results confirm that 2D graphene layers entrap MoO$_2$ nanoparticles homogeneously in the composite. X-ray photoelectron spectroscopy shows the presence of oxygen functionalities on graphene, which allows intimate contact between MoO$_2$ nanoparticles and the graphene. Conductive atomic force microscopy reveals an extraordinarily high nanoscale electronic conductivity for MoO$_2$/Graphene, greater by 8 orders of magnitude in comparison to bulk MoO$_2$. The layered nanostructure and the conductive matrix provide uninhibited conducting pathways for fast charge transfer and transport between the oxide nanoparticles and graphene which are responsible for the high rate capability, a large lithium ion capacity of 770 mAh g^{-1}, and an excellent cycling stability (550 mAh g^{-1} reversible capacity retained even after 1000 cycles!) at a current density of 540 mA g^{-1}, thereby rendering it to be superior to previously reported values for neat MoO$_2$ or MoO$_2$/Graphene composite. Impedance analyses demonstrate a lowered interfacial resistance for the composite in comparison to neat MoO$_2$. Our results demonstrate the enormous promise that MoO$_2$/Graphene holds for practical Li-ion batteries.

1. Introduction

Li-ion batteries are the rechargeable batteries of choice for high performance portable electronic devices. Research efforts are now dedicated towards increasing energy density and reducing cost

* Corresponding author. Tel.: +91 4023016024; fax: +91 40 23016003.
 E-mail address: mdeepa@iith.ac.in (M. Deepa).

while maintaining a high rate performance to enable their use for hybrid electric vehicles and power tool applications [1–3]. In order to realize an appreciable improvement in Li ion storage capacity, durability and rate capability, there is a quest for new cathode and anode materials that are environmentally benign, are capable of delivering high power densities and have the potential to endure a large number of charge–discharge cycles without undergoing degradation [4,5]. Typically, commercial Li-ion batteries use graphite as the anode material which is characterized by a theoretical specific capacity of 372 mAh g^{-1}. Graphite by the virtue of its layered structure allows a reversible Li-insertion and extraction reaction during discharging and charging, respectively. But a low specific capacity, as six carbon atoms are required to accommodate one Li ion and abuse tolerance issues from Li plating limit its performance [6,7]. To attain higher lithium storage capacities, several transition metal oxides such as Fe_3O_4, Co_3O_4, MoO_3, V_2O_5 and Fe_2O_3 capable of undergoing reversible Li^+ insertion/extraction reaction with more than 6 Li^+ ions per formula unit, have also been employed in the past as advanced alternates to graphite anodes, however, in spite of delivering high energy densities, these materials experience substantial volume variation during Li^+ insertion/extraction process, which leads to the pulverization of the electrode material and rapid decline of capacity [8].

To counter the aforementioned issues that adversely impact the anode's performance in Li-ion batteries, oxides in nanocrystalline forms are used, as a decrease in particle size leads to a decrease in the diffusion path length of Li^+ ion during ingress and egress phenomena thereby improving both capacity and cyclability [9,10]. Another alternate involves synthesis of composites of oxides with carbon; the latter enhances the electronic conductivity and as a consequence the overall battery performance [11], however, the carbon coating on the metal oxide is not sufficient to buffer the volume expansion and contraction incurred by oxides during charge/discharge processes. To address this concern, one dimensional monolayers of graphene with atomic thickness are useful as they exhibit a very high surface area (2600 m^2 g^{-1} per sheet), large thermal and electronic conductivities, chemical resistance and mechanical flexibility [12–14]. Graphene layers prevent both volume changes and aggregation of metal oxide nanoparticles during charge/discharge processes as the oxide nanoparticles are sandwiched between the sheets and therefore cannot agglomerate. Furthermore, the attachment of metal oxide or any other inorganic moiety on graphene effectively inhibits the restacking of graphene layers. In the past, composites of graphene with Fe_3O_4, Fe_2O_3, Co_3O_4, SnO_2 and TiO_2, have been attempted and they have shown higher capacity, rate capability and cyclability as compared to their bulk oxide counterparts [15–19].

Among transition metal oxides capable of functioning as anodes, nanostructured molybdenum dioxide (MoO_2) undergoes Li^+ insertion/extraction reactions with a concurrent four electron insertion/extraction and this corresponds to a theoretical specific capacity of 838 mAh g^{-1}. Among several reports on MoO_2 and composites [20–28] as a Li-ion battery anode material, a report on a MoO_2/Graphene composite by Sun and co-workers is noteworthy, as they achieved a reversible capacity of 342 mAh g^{-1} in the first cycle and a capacity of 598 mAh g^{-1} was acquired at the end of 70 cycles at a current density of 1000 mA g^{-1} [29]. But it must be mentioned that authors in [29] employed an elevated temperature process whereby they achieved a hierarchical assembly of MoO_2 nanoparticles and graphene layers. In the present study, we report a simple one pot *in-situ* low temperature solution phase reduction method which allowed a homogeneous embedding of MoO_2 nanoparticles in reduced graphene oxide nanosheets, thus allowing an intimate and direct contact between the two entities. Previous reports on MoO_2/Graphene or a transition metal oxide/Graphene

composite have largely employed hydrazine as a reducing agent for reducing graphene oxide to graphene which is highly toxic [17,29]. In the present report, we circumvented this issue by using non-toxic citric acid along with poly(ethylene glycol) to reduce graphene oxide to graphene, which is incidentally also a relatively inexpensive approach. By confining to a hydrothermal process for graphene formation and conversion of the metal oxide precursor to MoO_2, we were also able to perform the reaction at a low temperature. Furthermore, we also studied the role of citric acid in controlling the reduction of graphene oxide to graphene by preparing samples using a protocol devoid of citric acid. The MoO_2/Graphene composite and has been studied by X-ray diffraction (XRD), scanning electron microscopy (SEM), transmission electron microscopy (TEM), Raman spectroscopy and X-ray Photoelectron Spectroscopy (XPS) and conducting atomic force microscopy (C-AFM). The structural features of the composite and the remarkably high nanoscale current conduction capability of the composite have been correlated to the outstanding capacity, rate capabilities and cycling performance (when employed as an anode in a Li ion battery). We show, by rigorous experimentation that our values for MoO_2/Graphene composite are not only superior to reported values in literature based on MoO_2 or MoO_2/Carbon nanostructure anodes, but also considerably enhanced in comparison to neat graphene, neat MoO_2 and even MoO_2/Graphene oxide (the latter three prepared herein).

2. Experimental

2.1. Chemicals

Graphite flakes (Aldrich), Ammonium heptamolybdate ((NH_4)$_6$$Mo_7O_{24}$·4$H_2O$) (AHM) (99%, Merck), $KMnO_4$ (99%, Merck), poly(ethylene glycol) 400 (PEG 400, Merck) and citric acid anhydrous ($C_6H_8O_7$, 99.5%, Merck) were used as received. Reagents: H_2SO_4 (98%), H_3PO_4 (88%) and H_2O_2 (30%) of GR grade were purchased from Merck. Ultrapure water (resistivity = 18.2 MΩ cm) obtained through Millipore Direct-Q 3 UV system was used as solvent.

2.2. Preparation of graphene and MoO_2/Graphene

Graphene oxide (GO) was prepared by an improvised method [30,31], wherein graphite flakes (1.5 g) and $KMnO_4$ (9 g) was added slowly to a concentrated H_2SO_4/H_3PO_4 mixture (9:1 v/v) over a period of 30 min followed by continuous stirring for 12 h at 50 °C. The reaction mixture was poured onto a mixture of ice water (200 mL) and 30% H_2O_2 (3 mL). The solution was centrifuged for 1 h at 4000 rpm, and the supernatant liquid was decanted away. The centrifugate was again washed with water (100 mL) followed by 30% HCl (100 mL) and ethanol (100 mL) washes. Successive washings with water and ethanol were repeated twice and the resultant suspension was dried in vacuum for 12 h at 50 °C till a dry black solid of GO was isolated, which was stored in nitrogen. To a dispersion of GO (100 mg) in water (50 mL), 0.56 mM ammonium heptamolybdate ((NH_4)$_6$$Mo_7O_{24}$·4$H_2O$) in water (20 mL), citric acid and poly(ethylene glycol) (PEG) mixed in a 1:3 M ratio were added. The solution was placed in a 100 mL Teflon lined autoclave and heated in a vacuum oven at 180 °C for 26 h. The resulting black colored MoO_2/Graphene composite was filtered and washed with water, dried and stored in inert atmosphere. The optimization of the proportions of MoO_2 and graphene in the MoO_2/Graphene composite prepared herein, was done on the basis of electrochemical performances of composites prepared with varying MoO_2:Graphene weight ratios, which is shown in Fig. S1 (supporting information). The results presented in the report are

for the optimized MoO_2/Graphene composite. Further, to study the effect of citric acid in inducing the reduction of graphene oxide, a composite was prepared using the exactly same procedure, but without citric acid and the resulting product was designated as MoO_2/Graphene oxide (XRD pattern is shown in Fig. S2, supporting information). The synthesis of neat MoO_2 and neat graphene are provided in supporting information. Neat graphene was the product obtained after hydrothermal processing of GO with poly(ethylene glycol) and citric acid.

Working electrodes were prepared by mixing 80 wt. % of active material (MoO_2/Graphene or neat MoO_2 or graphene or graphene oxide or MoO_2/Graphene oxide), 10 wt. % acetylene black and 10 wt. % poly(vinylidene difluoride) with a few drops of N-methyl pyrrolidine. The resultant slurry in each case was coated on 13 mm stainless steel foils and dried at 80 °C for 12 h in vacuum oven for expunging the solvent. Swagelok cells were employed for electrochemical measurements and these were assembled inside an argon filled glove-box (O_2 and H_2O concentration ≤ 1 ppm and 0.5 ppm). A lithium foil was used as a counter/reference electrode and a Whatman glass microfiber filter paper functioned as the separator. The electrolyte was 1 M $LiPF_6$ dissolved in a mixture of ethylene carbonate and propylene carbonate (1:1 v/v).

2.3. Characterization techniques

Galvanostatic charge−discharge measurements were performed on a battery testing unit (Arbin Instruments, BT 2000) at different current densities in the range of 0.01−3 V versus Li/Li$^+$ at room temperature. Cyclic voltammetry of the electrodes was performed on an Autolab PGSTAT 302N coupled with NOVA 1.7 software. X-ray diffraction on the electrodes was performed on XRD, PANalytical, X'PertPRO instrument with Cu-Kα (λ = 1.5406 Å) radiation. A Bruker Senterra dispersive micro Raman spectrometer with a 532 nm laser was used for recording Raman spectra. Brunauer−Emmett−Teller (BET isotherm Quantachrom 2200) technique was used for surface area measurements. Scanning electron microscopy (Hitachi S-4300 SE/N) and transmission electron microscopy (TECNAI G-20, 200 keV, FEI) was carried out on the composites. Conductive AFM (C-AFM, Veeco, Multimode 8 with ScanAsyst and Nanoscope 8.10 software) was used for recording simultaneous topography and current images in contact mode. Cantilevers made of Sb doped Si (n-doped; resistivity = 0.01−0.025 Ω cm) and coated with Pt/Ir (20 nm) on the front and backside were obtained from Veeco. Spring constant of tip was 0.2 N m^{-1} and a load force of 48 nN was

maintained between the tip and the sample. The MoO_2/Graphene composite deposited on a stainless steel substrate, (area = 13 mm^2) was mounted on the scanner, using conductive carbon tape. Silver paste was applied for electrical contacts along the cross-section of this assembly. The AFM tip is scanned in contact with the sample surface for imaging currents and simultaneously topography was also obtained. A dc bias of 1 V was applied to the tip and the sample is held at ground potential. Nanoscale point contact I−V curves were recorded by the ramping the potential between −10 and +10 V, on different spots on the current image.

3. Results and discussion

3.1. X-ray diffraction and Raman spectra

XRD patterns of the neat MoO_2, neat graphene and MoO_2/Graphene composite are shown in Fig. 1. The XRD pattern of the MoO_2/Graphene composite shows intense well-resolved peaks at d = 3.42, 2.44 and 1.71 Å corresponding to (110), (200) and (220) planes of monoclinic MoO_2 with Space Group: P2$_1$/c(14), in concordance with JCPDF: 86-0135, thus indicating that the crystal structure of MoO_2 is preserved in the composite. The Raman spectra of graphene oxide and MoO_2/Graphene composite are shown in Fig. 2. The Raman spectrum of neat graphene oxide shows the D band, attributable to surface defects at 1350 cm^{-1} and the G peak at 1588 cm^{-1} which is ascribed to the in-plane vibration of sp^2 hybridized carbon atoms. The lower intensity of the D-band relative to the G-band, shows that the defect concentration in pristine graphene oxide is low, which is advantageous for improving conductive properties. In the Raman spectrum of MoO_2/Graphene, the D and G bands are retained, albeit the relative intensities are reversed vis-a-vis neat graphene oxide. The positions of the D and G bands are also downshifted to 1309 and 1585 cm^{-1}, indicating the conversion of graphene oxide to graphene upon composite formation. It must be recalled that this is the Raman spectrum of the product (labeled by us as MoO_2/Graphene) formed after the hydrothermal processing of GO, molybdenum salt, citric acid and poly(ethylene glycol). In addition, strong intense peaks are observed at 816 and 988 cm^{-1}, attributable to ν(Mo−O−Mo) and ν(Mo=O) stretching modes of MoO_2, clearly affirming the inclusion of MoO_2 in graphene. The inset of Fig. 2 shows the Raman spectrum of neat graphene oxide and MoO_2/Graphene Oxide composite. Since the positions of D and G bands ongoing from the graphene oxide to the MoO_2/Graphene oxide composite show no difference, it is apparent, that citric acid is essential to bring about the reduction of GO to graphene. For if it had been otherwise, then this product obtained after processing GO, molybdenum salt with
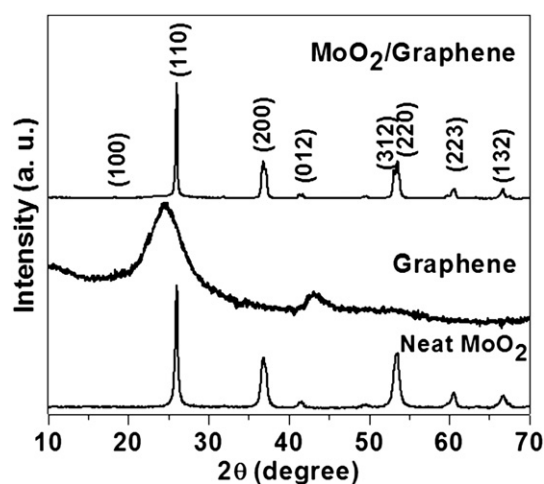

Fig. 1. XRD patterns of neat MoO_2, neat graphene and MoO_2/Graphene composite.
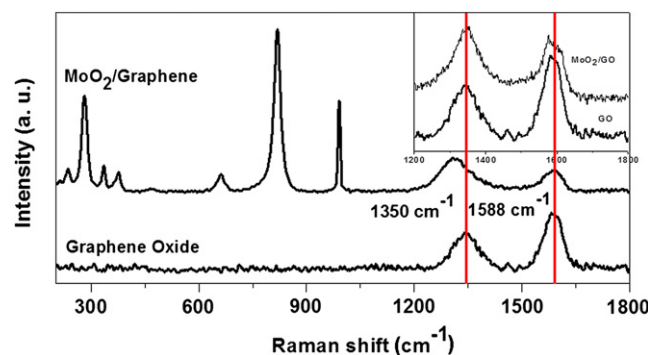

Fig. 2. Raman spectra of MoO_2/Graphene and graphene oxide; the solid lines pass through the D and G bands in graphene oxide. Inset shows a comparison of Raman spectra of MoO_2/Graphene oxide and graphene oxide.

poly(ethylene glycol), which has been labeled by us as MoO_2/Graphene oxide, should have shown downshifted D and G bands relative to GO as observed for the product (labeled by us as MoO_2/Graphene) obtained by using the same reactants, along with citric acid. It is apparent that citric acid is essential to bring about the reduction of GO to graphene.

3.2. Electron microscopy

SEM images of neat graphene, neat MoO_2 and MoO_2/Graphene composite are shown in Fig. 3. Stacks of overlapping graphene nanosheets with foldings and wrinkles which are characteristic of graphene, can be seen in Fig. 3a and b [32]. The large graphene sheets prefer to roll up to acquire entangled structures due to their inability to retain a high aspect ratio two-dimensional structure. Similar three-dimensional flaky structures for graphene are well-reported [33]. We could however identify monolayers of graphene by TEM. The image of neat MoO_2 shows an interconnected framework of MoO_2 grains of irregular shapes (Fig. 3c). The grains are compactly packed and they tend to form large aggregates. The low magnification image of the MoO_2/Graphene composite is representative of graphene than of MoO_2, as it shows mingling closely packed thick flakes of graphene with

well-defined edges that seem to be protruding outwards. The wavy crumpled nature of graphene platelets is retained in the composite and a closer inspection of the high magnification image (Fig. 3e) shows the MoO_2 grains to be uniformly entrenched in the graphene oxide nanosheets. The low temperature hydrothermal route adopted in this report, for combining MoO_2 with graphene allows the formation of a composite, wherein a direct contact between the two moieties could be achieved. Such an intimate connectivity between MoO_2 nanoparticles and graphene plays a significant role in improving the electronic conduction properties of the composite, thus promoting charge transport and transfer during charge/discharge cycles. The slight difference in contrast and morphology relative to that obtained for neat graphene is also an indicator to MoO_2/Graphene composite formation. Direct evidence for successful formation of the composite was obtained through elemental mapping and energy dispersive X-ray analysis (EDS) results which are collected in Fig. 3f. The elemental maps of carbon, oxygen and molybdenum collected from the SEM image of the composite shown in Fig. 3d, clearly delineate a uniform and homogeneous distribution of the three elements across the specimen, thus confirming the co-existence of Mo with C and O; the latter two being the principal constituents of graphene oxide. EDS pattern also shows prominent signals due
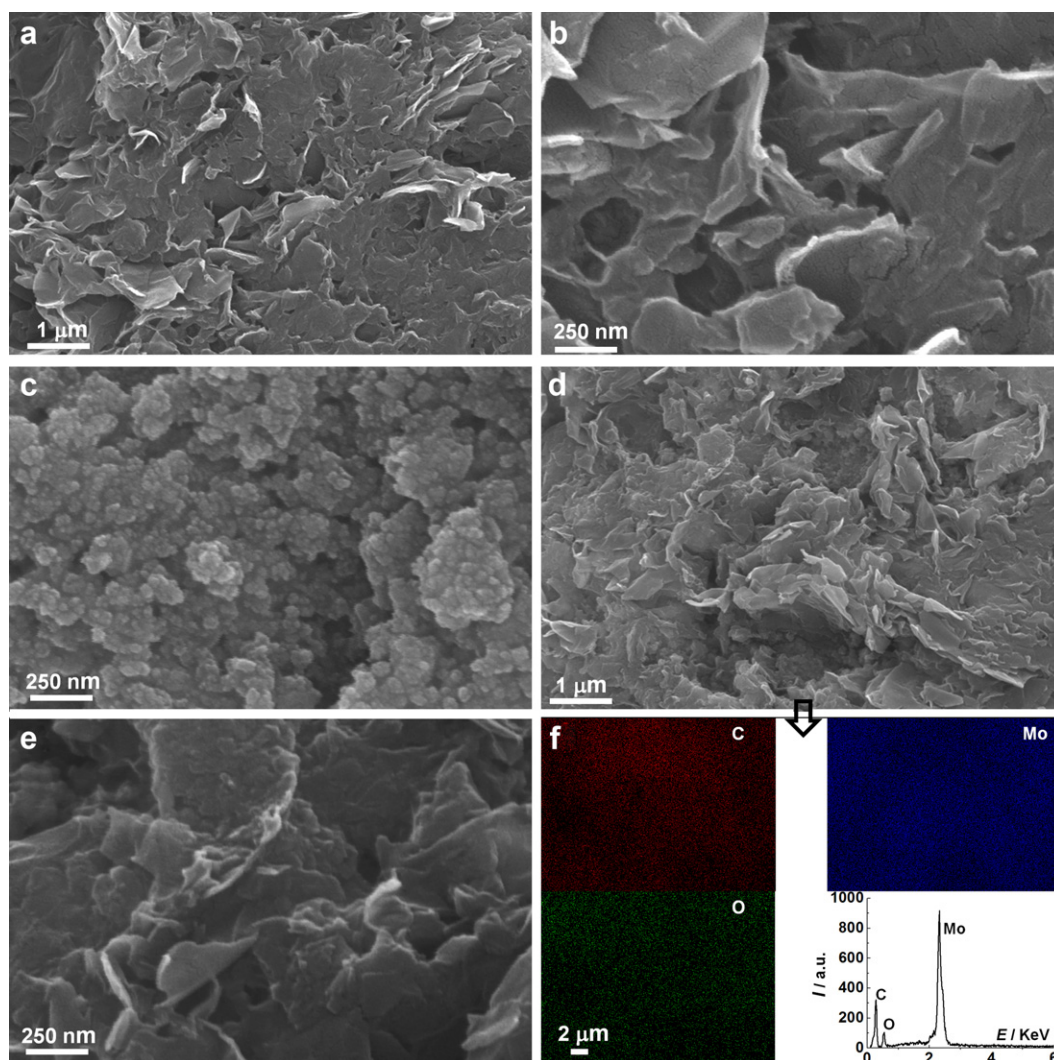
Fig. 3. SEM images of graphene oxide at (a) low and (b) high magnifications, (c) neat MoO_2, (d) low and (e) magnification images of MoO_2/Graphene and (f) elemental maps of S, O and C in MoO_2/Graphene and an EDS plot of MoO_2/Graphene.

to C, O and Mo, again affirming the successful integration of MoO_2 with graphene.

The TEM micrographs of neat graphene, MoO_2 and MoO_2/Graphene composite are shown in Fig. 4. The presence of few-layer graphene with well-defined edges, and the silk veil like texture of the nanosheets is also discernible from Fig. 4a and b. The nanosheets appear to spread over a few microns in length, indicating that the exfoliated sheets even after chemical reduction, are able to retain a high aspect ratio. The sheets are tangled, which is a signature of mono- or few-layer graphene [33]. Bright field image of neat MoO_2 (Fig. 4c) shows densely packed agglomerates of MoO_2. The nano-platelet morphology of graphene is best suited for forming composites with a transition metal oxide as it can easily accommodate a large quantity of the electroactive intercalant: MoO_2, which can easily slide between the nanosheets and remain entrapped therein by the virtue of electrostatic interactions between the positively charged metal ion, Mo^{4+} and the negatively charged carboxylate groups and the oxygens on the epoxy and hydroxyl groups, which are flanked to the graphene sheets. The TEM images of the composite (Fig. 4d) show that the MoO_2 grains are indeed embedded in the nanosheets of graphene and the fact that these oxide grains are homogeneously implanted in the graphene oxide nanosheets is evidenced from Fig. 4f, wherein

a uniform and continuous coverage of the nanosheets by MoO_2 is attained. Well-defined plane facets of MoO_2 can also be seen in some regions of the composite (Fig. 4e), indicating a preferred orientation for these crystallites.

3.3. X-ray photoelectron spectroscopy and conducting-AFM

XPS survey and core level spectra of MoO_2/Graphene composite are shown in Fig. 5. The survey spectrum (Fig. 5a) of the composite shows distinct signals at 232.9, 284.3, 397.7, 415.1 and 531.2 eV which are assigned to the Mo3d, C1s, $Mo3P_{3/2}$, $Mo3P_{1/2}$ and O1s respectively; indicating the contributions from both MoO_2 and graphene. The asymmetrical profile of the C1s signal (Fig. 5b) reflects different chemical environments for carbon, which obviously stems from the presence of different oxygen containing groups associated with carbon atoms on graphene. The deconvoluted C1s spectrum shows four components and these are ascribed to C—C bonds at 284.6 eV, C—O groups at 286.2 eV, C=O groups at 287.5 eV and the O—C=O moieties at 288.8 eV. The deconvoluted Mo3d core level spectrum (Fig. 5c) shows four peaks; with the lower energy spin—spin doublet due to the +4 oxidation state of the Mo, at 232.19 and 229.06 eV due to $Mo^{IV}3d_{3/2}$ and $Mo^{IV} 3d_{5/2}$. The higher energy, lower intensity peaks (in comparison to Mo^{IV} peaks) at 234
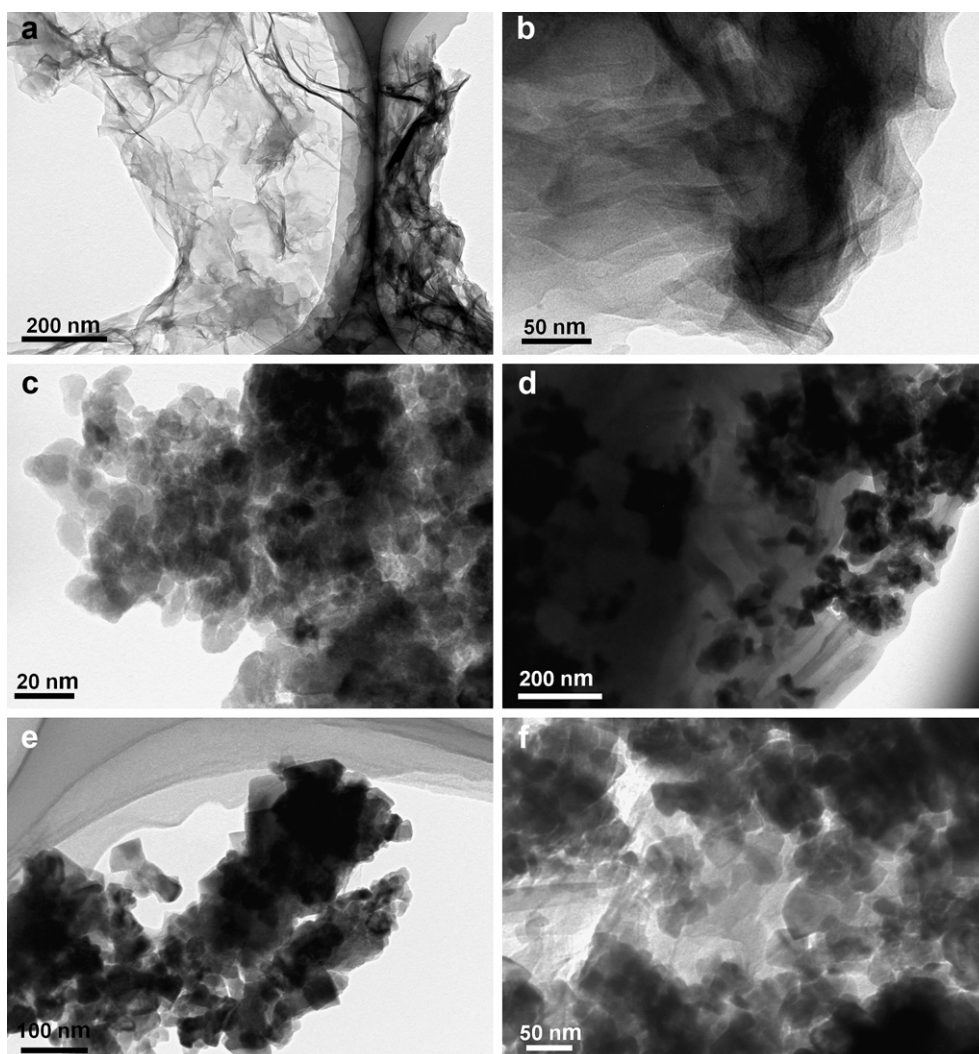
Fig. 4. TEM micrographs of graphene at (a) low and (b) high magnifications, (c) neat MoO_2, (d,e,f) MoO_2/Graphene composite at different magnifications; plane facets of MoO_2/Graphene crystallites with well-defined shapes can be seen in e and f.
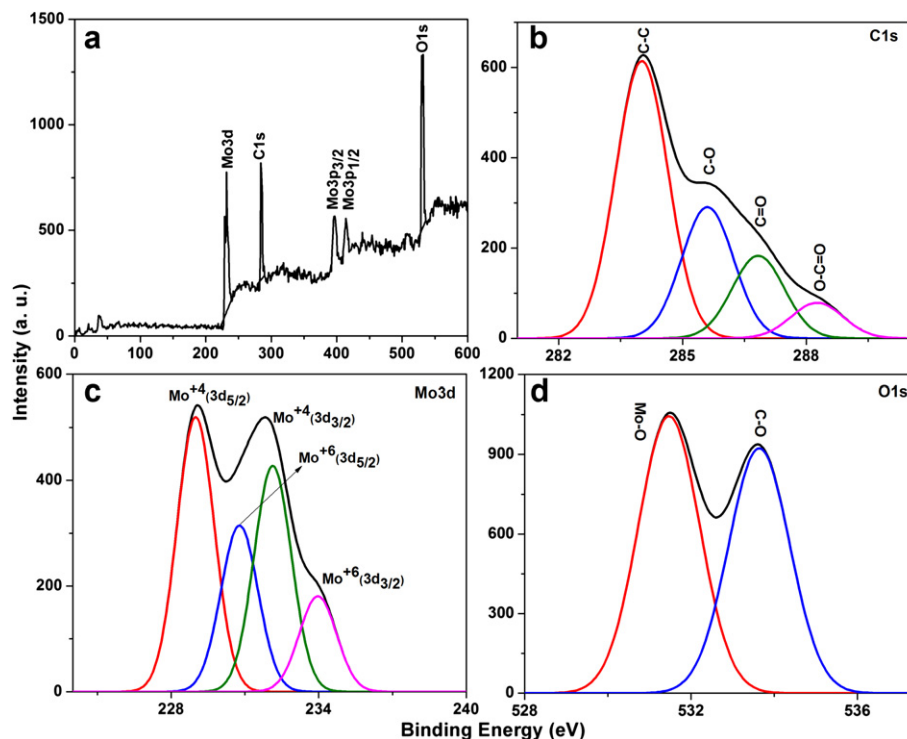
Fig. 5. XPS (a) survey spectrum of MoO_2/Graphene and deconvoluted core level (b) C1s, (c) Mo3d and (d) O1s of MoO_2/Graphene.

and 230 eV arise from Mo^{VI} $3d_{3/2}$ and Mo^{VI} $3d_{5/2}$ of MoO_3 resulting from the slight surface oxidation of metastable MoO_2 in air. The O1s core level spectrum shows two deconvoluted contributions at 533.6 and 531.5 eV, corresponding to residual oxygen bonded to carbon in graphene and oxygen associated with MoO_2 respectively (Fig. 5d). The oxygen content in reduced graphene oxide was determined by integrating the area of the curves in the XPS core level C1s spectrum of the composite (Fig. 5b) which represents the contributions from C–O groups (C=O, C–O, O–C=O). The area thus obtained is divided by the sensitivity factor to yield the oxygen content. The oxygen content is deduced to be 25.4% which is adequate for an effective interaction between MoO_2 nanoparticles and graphene nanosheets. The core level spectra again provide conclusive evidences for incorporation of MoO_2 nanoparticles in graphene monolayers.

Current image of the MoO_2/Graphene composite (Fig. 6a) obtained by C-AFM shows the presence of interconnected conducting domains spread over regions of about few micron dimensions (bright regions), and the maximum current is remarkably high ($\sim$1.2 μA) contrasting against an i_{max} of only 7×10^{-5} μA in neat MoO_2 (Fig. 6b). Such an enormous differential by almost five orders of magnitude reflects the high current carrying capacity of the composite, beneficial for charge transport. The regions enclosed in circles show dull spots (corresponding to currents of $\sim$0.6 μA) connecting the bright regions, are suggestive of conductive interconnects between the large conducting domains. Neat MoO_2 is almost insulating relative to MoO_2/Graphene and this is again reinforced from the representative point contact I–V curves averaged over 15 spots (Fig. 6a$'$ and b$'$), and the nanoscale conductivity of MoO_2/Graphene deduced from the linear portion of the curve, is 3.9 S cm^{-1} compared to a value of 2.7×10^{-8} S cm^{-1} in neat MoO_2. It is apparent that such a massive increase in conductivity by 8 orders, upon including graphene, can dramatically transform the electrochemical capabilities of MoO_2. Here, the use of a low temperature synthetic route for preparing the composite enabled the formation of an intimate contact between the highly conducting graphene

nanosheets and the MoO_2 nanoparticles. A direct contact between the two nanoparticles allows seamless transfer and transport of Li^+ ions and electrodes through the bulk of the electrode and when combined with the high effective surface area of composite, due to the nano layered structure of MoO_2 which permits greater Li^+ ion uptake compared to neat graphene or neat MoO_2, a remarkably high Li^+ ion storage capacity results.

3.4. Electrochemical charge–discharge studies

Cyclic voltammograms of MoO_2/Graphene composite and neat MoO_2 recorded at a scan rate of 0.1 mV s^{-1} are displayed in Fig. 7. For the composite (Fig. 7b), in the first cycle, two reduction peaks in the cathodic branch are observed at 1.28 and 1.56 V which are ascribed to the phase transition of partially lithiated Li_xMoO_2 from orthorhombic to monoclinic during Li-insertion, as reported previously by Dahn and McKinnon [26]. An irreversible broad peak is also seen at 0.7 V, which can be attributed to the reduction of electrolyte solution and formation of a passivation layer at the anode surface, as this peak disappears in the subsequent cycles. In the ensuing cycles two redox couples located at 1.56/1.68 V and 1.28/1.39 V are observed which are due to the phase transitions of the partially lithiated Li_xMoO_2. The CV plots for MoO_2 also show oxidation/reduction couples at 1.52/1.73 V and 1.26/1.51 V (Fig. 7a), corresponding to phase transitions of partially lithiated Li_xMoO_2. The CV plots of the MoO_2/Graphene composite acquire stability in the 2nd cycle itself, as in the following cycles the curve retraces the plot obtained in the previous scan. The CV curves of the neat MoO_2 shrink with cycling, which indicates that Li^+ intercalation and de-intercalation is not as reversible in MoO_2 as in the MoO_2/Graphene composite.
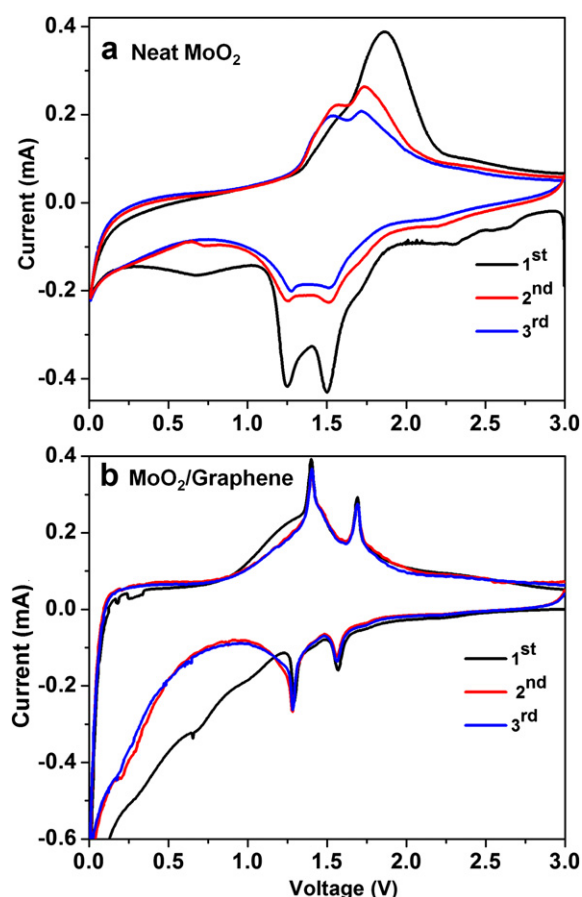
The charge–discharge curves for an as-fabricated MoO_2/Graphene electrode in the first cycle and the subsequent cycling behavior measured between 0.01 and 3.0 V *versus* Li metal at a current density of 540 mA g^{-1} is shown in Fig. 8a. In the first cycle,
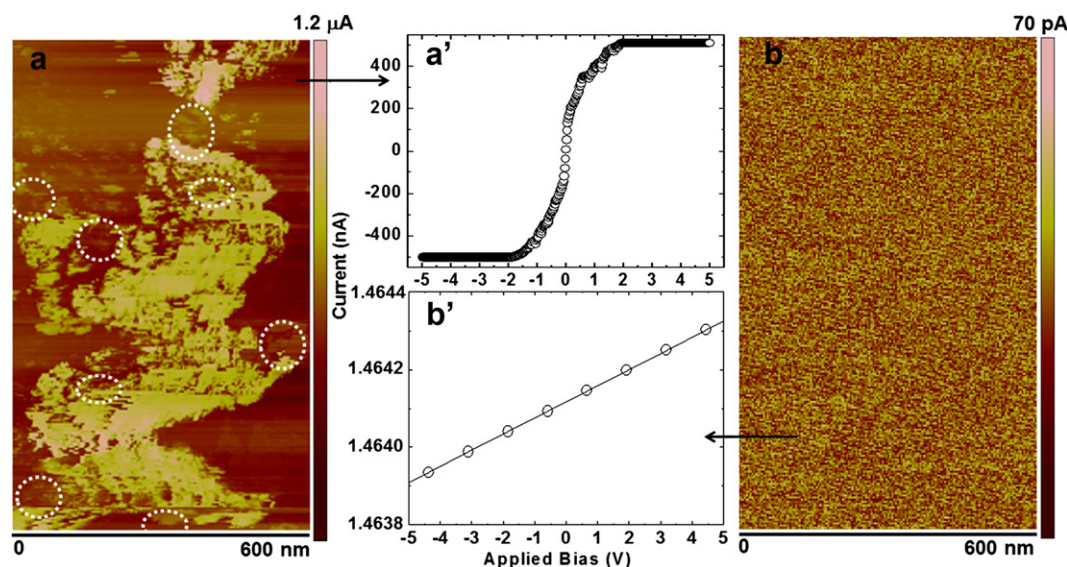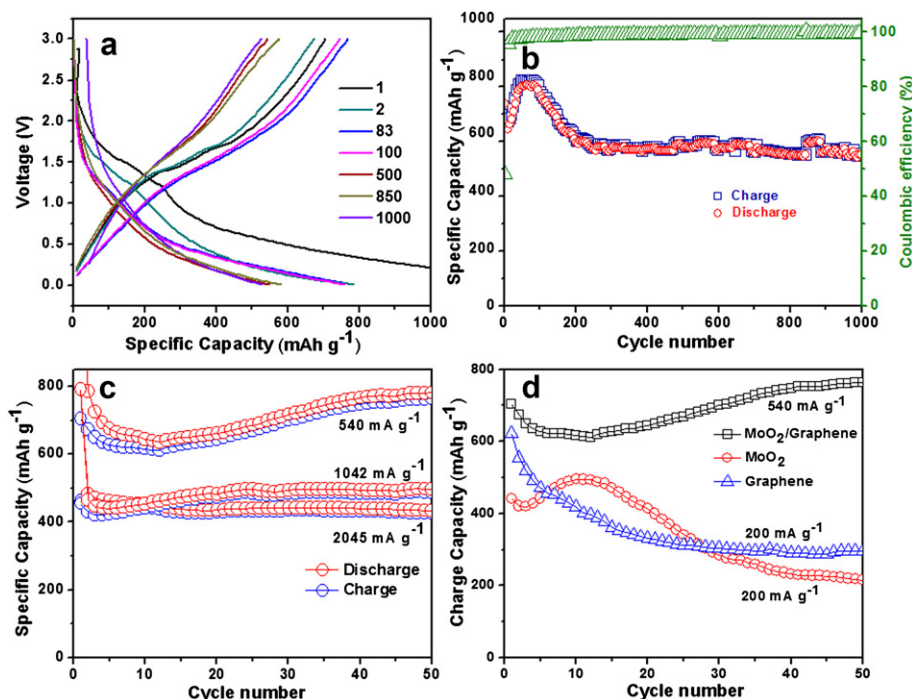
Fig. 6. Current images of (a) MoO_2/Graphene and (b) neat MoO_2 obtained from C-AFM. Representative point contact nanoscale I–V characteristics of (a′) MoO_2/Graphene and (b′) neat MoO_2 obtained from the current image.

two short discharge plateaus at 1.52 and 1.25 V and two charge plateaus at 1.69 and 1.41 V were observed and these are in agreement with the CV curves. On the basis of the composition of the as-synthesized MoO_2/Graphene electrode, which is: 66.8% of MoO_2 and 33.2% of graphene, the theoretical specific capacity of the MoO_2/Graphene composite is deduced to be 766.8 mAh g^{-1} (see supporting information). For the initial cycle, MoO_2/Graphene composite electrode delivers discharge and charge specific capacities of 1450 and 703.7 mAh g^{-1} respectively which corresponds to an irreversible capacity loss of 52%. The high irreversible capacity loss for composite electrodes is due to the following reasons: the conversion of graphene oxide to graphene is not absolute, even by the use of citric acid as core level XPS spectrum of C1s reveals the presence of oxygen functionalities. These oxygen containing groups on graphene layers can irreversibly entrap Li^+ ions. To support this point we have also measured charge–discharge characteristics of neat graphene and the first cycle shows discharge and charge capacities of 1386.5 and 623 mAh g^{-1} respectively which correspond to an irreversible capacity loss of 55% (Fig. S3, supporting information). Other possible reasons include decomposition of electrolyte and formation of solid electrolyte interface [19]. The cyclability of MoO_2/Graphene composite and the columbic efficiency of this electrode measured at a current density of 540 mA g^{-1} is shown in Fig. 8b. The composite shows a gradual increase in capacity up to 83 cycles; and at this juncture, it shows a reversible capacity of 769.3 mAh g^{-1} coupled with an excellent columbic efficiency of ∼98%. From 83 cycles onwards up to few cycles the capacity gradually decreases and thereafter it remains stable with increasing number of cycles, and at the end of 1000 charge–discharge cycles, the MoO_2/Graphene electrode still shows a reversible capacity of 530 mAh g^{-1} with a coulombic efficiency close to 100%. The electrode retains 75.4% of its initial capacity at the end of 1000 repetitive cycles, indicating its stability for Li^+ insertion and extraction. The MoO_2/Graphene electrode also shows outstanding rate capabilities (Fig. 8c) wherein the charge–discharge capacities at different C rates of 540, 1042 and 2045 mA g^{-1} were plotted. At 1042 mA g^{-1}, after 50 cycles the composite electrode shows a reversible capacity of 497 mAh g^{-1}. At a still higher current density of 2045 mA g^{-1} the electrode shows an initial reversible capacity of 460 mAh g^{-1} which is much superior to previously reported values on MoO_2/Graphene composite [29], wherein authors achieved a value of 407 mAh g^{-1} at 2000 mA g^{-1} current density after 70 cycles. At the same C-rate, after subjecting the MoO_2/Graphene electrode to 50 cycles, a charge

Fig. 7. Cyclic voltammograms of (a) neat MoO_2 and (b) MoO_2/Graphene electrodes *versus* metallic Li in the +0.01 to +3.0 V potential range.

Fig. 8. (a) Galvanostatic discharge–charge curves of the MoO_2/Graphene composite electrode at a current density 540 mA g^{-1} in the voltage range of 0.01–3.0 V, (b) the cycling performance of the MoO_2/Graphene at current density of 540 mA g^{-1}; (c) rate performance of the MoO_2/Graphene composite and (d) the cycling performance of MoO_2/Graphene, neat MoO_2 and neat graphene electrodes at different current densities.

capacity of 427 mAh g^{-1} is retained. The MoO_2/Graphene oxide (Fig. S4, supporting information) electrode shows a reversible capacity of 605 mAh g^{-1} in the initial cycle at current density of 540 mA g^{-1} and upon increasing the current density to 2045 mA g^{-1} the electrode shows a reversible capacity of 300 mAh g^{-1}. The high capacity and improved rate capability of MoO_2/Graphene as opposed to that shown by MoO_2/Graphene oxide, are a clear indicators of the fact that fewer number of oxygen containing functionalities on the graphene layers improves the conduction capability and allow un-hindered ion and electron transport in the composite. The superior performance of MoO_2/ Graphene was also realized by comparing the reversible charge capacity of this electrode with that of the individual components (namely, neat graphene and neat MoO_2) at current densities of 200, 200 and 540 mA g^{-1} and these plots recorded as function of number of cycles are displayed in Fig. 8d. For neat graphene the initial capacity (602 mAh g^{-1}) is close to that MoO_2/Graphene electrode; however this capacity for neat graphene shrinks to about 300 mAh g^{-1} after enduring 50 cycles. For neat MoO_2 electrode, the reversible capacity in the first cycle is 442 mAh g^{-1} and it goes through a maximum of 495 mAh g^{-1} (in the 10th cycle) and upon further cycling, the capacity monotonically decreases to about 215 mAh g^{-1} (in the 50th cycle). For the MoO_2/Graphene electrode the initial capacity (703.7 mA h g^{-1}) is higher than that of neat graphene or neat MoO_2 even at a much higher current density of 540 mA g^{-1}. The higher capacity of MoO_2/Graphene as compared to neat MoO_2 can also be correlated to the higher surface area of the composite (50.4 m^2 g^{-1}, measured by BET). This value is 4.5 times higher than that of neat MoO_2 (10.9 m^2 g^{-1}).

3.5. Ex-situ XRD analyses and impedance spectra

The *ex-situ* diffractogram of the MoO_2/Graphene electrode during the 1st discharge at 1.5, 1.1 and 0.01 V was shown in Fig. 9a. At 1.5 V the XRD pattern is similar to that of the as-synthesized

composite electrode albeit a single downshift of the peak corresponding to the (110) plane. This implies that the electrode does not undergo any phase transformation, whereas at 1.1 V, a new phase appears along with the parent monoclinic phase, at $d = 3.537$ and 1.8065 Å, which is suggestive of a possible two phase reaction. After subjecting to complete discharge at 0.01 V, the XRD pattern is characteristic of a single phase due to $Li_{0.98}MoO_2$. The *ex-situ* XRD patterns recorded intermittently during the cycling of the MoO_2/ Graphene electrode (Fig. 9b) shows that as the number of cycles increases the intensity of main peaks decreases and after 70 charge–discharge cycles the crystal structure of composite electrode becomes amorphous. The amorphous structure formation could enhance the Li$^+$ diffusion kinetics which in all likelihood is responsible for the retention of a high Li$^+$ ion capacity as a function of cycling [20,21,28,34]. The slight decrease in capacity with cycling (observed in Fig. 8b, above 200 cycles) could be due to the huge volume variation and/or agglomeration of the active oxide particles and as a consequence capacity fades in a manner similar to other metal oxides [8]. The *ex-situ* XRD pattern of the MoO_2/Graphene electrode after subjecting it to 1000 cycles shows unidentified small peaks, which could be due to the formation of an unknown phase. The *ex-situ* XRD patterns recorded for the same MoO_2/Graphene electrode after subjecting it to 50 charge–discharge cycles, at different C-rates of 540, 1042 and 2045 mA g^{-1} are shown in Fig. S5 (supporting information). The *ex-situ* XRD pattern reveals that even at a high C-rate of 2045 mA g^{-1}, and after 50 cycles, although the electrode is pre-dominantly amorphous, but traces of the monoclinic crystal structure are seen.
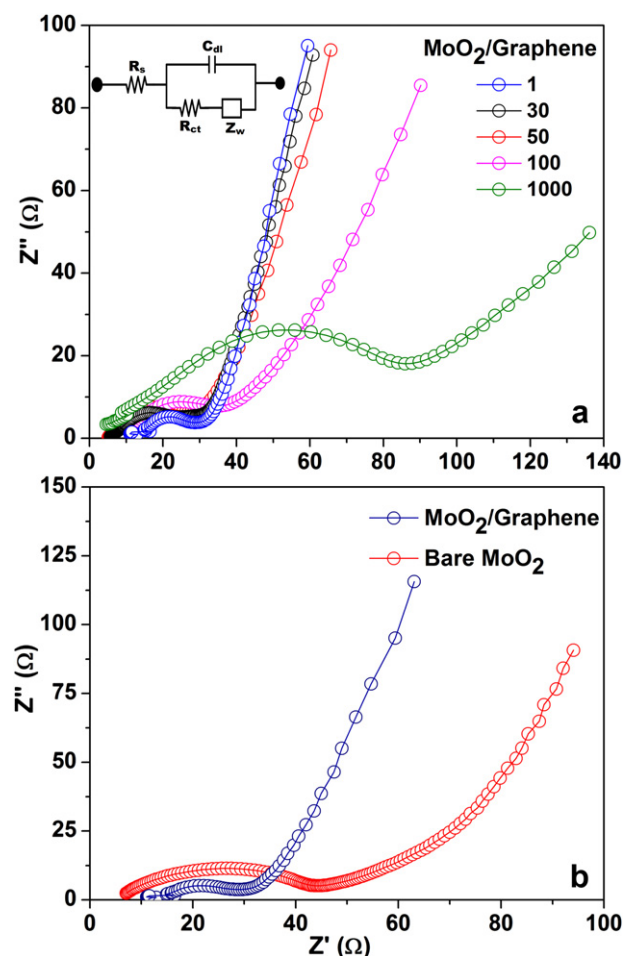
Nyqvist plots of MoO_2/Graphene composite as a function of cycling are shown in Fig. 10a and a comparison of the Z″ versus Z′ plots of neat MoO_2 and MoO_2/Graphene composite are shown in Fig. 10b. All plots generally comprise one depressed semicircle followed by an inclined straight line portion which appears in the low frequency range. The equivalent circuit displayed in Fig. 10a was found to give excellent fits almost over the entire frequency
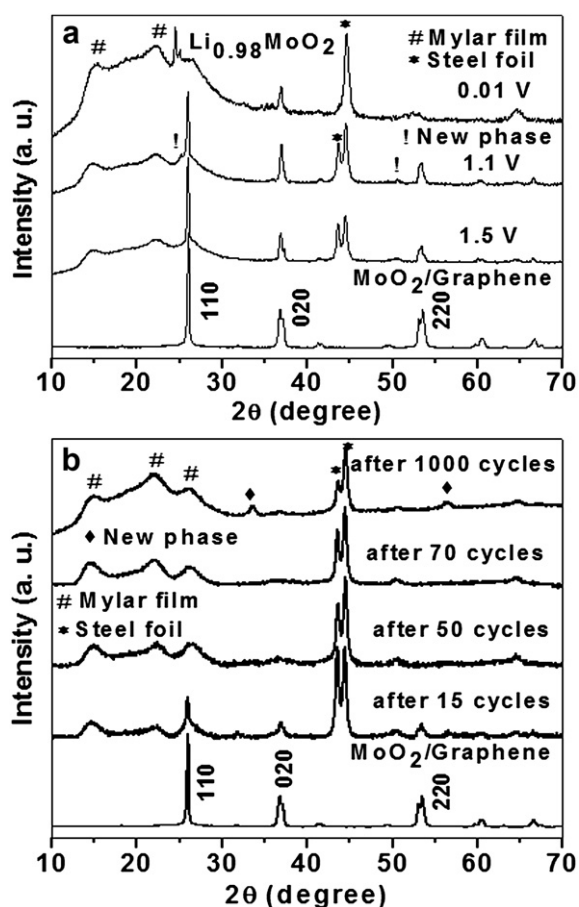
Fig. 9. *Ex-situ* XRD patterns of (a) MoO$_2$/Graphene recorded intermittently during the first discharge cycle, when the cell voltage reduced to 1.5, 1.1 and 0.01 V and (b) MoO$_2$/Graphene before cycling and after subjecting it to 15, 50, 70 and 1000 charge–discharge cycles.

Fig. 10. Nyqvist plots recorded under an ac amplitude of 10 mV superimposed over a zero dc bias for cells based on (a) MoO$_2$/Graphene as the working electrode at different stages of charge–discharge cycling and (b) MoO$_2$ and MoO$_2$/Graphene as the working electrode in the as-fabricated state. Metallic Li served as counter electrode and 1 M LiPF$_6$ in EC/PC as electrolyte for all plots. Inset of (a) shows the Randles equivalent circuit used for fitting the experimental data.

range of 10 mHz–100 kHz under consideration. The semicircle is attributed to a parallel combination of charge transfer resistance (R_{CT}) and electrical double layer capacitance (C_{dl}), while the linear portion stems from diffusion of ions/electrons through the bulk of the electrode material. The width of the semi-circle increases with cycling for the composite and this corresponds to an R_{CT} increase from 28 to 111 Ω cm^{-2} ongoing from an as-fabricated electrode to the one cycled a thousand times. It is evident since the R_{CT} does not increase by orders of magnitude after 1000 cycles, the Li$^+$ ion storage capacity does not decline steeply, and this was also observed in the cycling performance curve (Fig. 8b). The C_{dl} also shows a change from 5 to 3 F cm^{-2}. The slope of straight line portion in the low frequency regime does not change significantly over 50 cycles, and since the angle which it makes with the abscissa is close to 90°, the inference that can be drawn is that the electrode remains highly capacitive for about 50 cycles. At the end of 1000 cycles, the straight line portion acquires the ideal 45° slant of the classical finite length Warburg diffusion process, which indicates a decrease in the capacitive contribution to diffusion of ions through the electrode. On comparing the response of neat MoO$_2$ with that of MoO$_2$/Graphene (Fig. 10b), we find that the amplitude of the high frequency semicircle, is larger for neat MoO$_2$, corresponding to a R_{CT} of 44 Ω cm^{-2} and the linear portion signifies a diffusion controlled movement of ions, through the bulk of this electrode. On the contrary, R_{CT} is only 28 Ω cm^{-2} for the composite and the straight line portion shows the composite to be more capacitive. The superior capacitive character and the lower interfacial resistance of the MoO$_2$/Graphene composite are indirect measures of the ease of charge transfer across the electrolyte/electrode interface and the enhanced ability of this electrode to uptake charges. The nano-layered morphology of the composite allows greater charge intercalation and since graphene is an intrinsic electronic conductor, charge transfer/transport in the composite is also facilitated. These benefits cannot be realized in neat MoO$_2$ as it is bereft of any such electron conducting moiety or a nanostructured morphology.

4. Conclusions

A MoO$_2$/Graphene composite is synthesized by a hydrothermal route, involving the *in-situ* reduction of the molybdenum salt precursor and embedding of MoO$_2$ nanoparticles on graphene sheets in a single step. Electron microscopy, XPS and *ex-situ* XRD analyses confirm the homogeneous distribution of metal oxide nanoparticles in a 2D network of graphene sheets. The graphene layers prevent the aggregation of MoO$_2$ nanoparticles thus reducing volume expansion during cycling and the MoO$_2$ nanoparticles due to their confinement to graphene layers inhibit the layers from stacking. Such a concerted interplay between the two moieties, effectively manifest in a remarkably high lithium ion storage capacity, rate capability and cycling performance relative to

the neat oxide or carbon nanostructure based composites prepared by other methods. Further the nanoscale current images show a significantly amplified current carrying capability for the composite, induced by graphene and impedance spectroscopy reveals a lower resistance to charge transfer and transport for the MoO_2/Graphene composite in comparison to neat MoO_2, which are responsible for enhanced capacity and better endurance. Our results pave way for fabricating electrodes based on graphene/metal oxide composites, for realizing significant improvements in Li-ion storage performance in batteries.

Acknowledgments

Appendix A. Supporting information

Supplementary data related to this article can be found online at doi:10.1016/j.jpowsour.2012.05.050.

References

[1] B. Kang, G. Ceder, Nature 458 (2009) 190–193.
[2] A.S. Arico, P. Bruce, B. Scrosati, J.M. Tarascon, W.V. Schalkwijk, Nat. Mater. 4 (2005) 366–377.
[3] M. Armand, J.M. Tarascon, Nature 451 (2008) 652–657.
[4] J.B. Goodenough, Y. Kim, Chem. Mater. 22 (2010) 587–603.
[5] J.M. Tarascon, M. Armand, Nature 414 (2001) 359–367.
[6] N. Kambe, M.S. Dresselhaus, G. Dresselhaus, S. Basu, A.R. McGhie, J.E. Fischer, Mater. Sci. Eng. 40 (1979) 1–4.
[7] K. Guo, Q. Pan, S. Fang, J. Power Sources 111 (2002) 350–356.
[8] J. Cabana, L. Monconduit, D. Larcher, M. Rosa Palacín, Adv. Mater. 22 (2010) E170–E192.
[9] L. Ji, Z. Lin, M. Alcoutlabi, X. Zhang, Energy Environ. Sci. 4 (2011) 2682–2699.
[10] P.G. Bruce, B. Scrosati, J.M. Tarascon, Angew. Chem. Int. Ed. 47 (2008) 2930–2946.
[11] Li. Huiqiao, H. Zhou, Chem. Commun. 48 (2012) 1201–1217.
[12] S. Stankovich, D.A. Dikin, R.D. Piner, K.A. Kohlhaas, A. Kleinhammes, Y. Jia, Y. Wu, S.T. Nguyen, R.S. Ruoff, Carbon 45 (2007) 1558–1565.
[13] A.K. Geim, K.S. Novoselov, Nat. Mater. 6 (2007) 183–191.
[14] Alexander A. Balandin, S. Ghosh, W. Bao, I. Calizo, D. Teweldebrhan, F. Miao, C.N. Lau, Nano Lett. 8 (2008) 902–907.
[15] B. Li, H. Cao, J. Shao, G. Li, M. Qu, G. Yin, Inorg. Chem. 50 (2011) 1628–1632.
[16] D. Wang, D. Choi, J. Li, Z. Yang, Z. Nie, R. Kou, D. Hu, C. Wang, L.V. Saraf, J. Zhang, I.A. Aksay, J. Liu, ACS Nano 3 (2009) 907–914.
[17] X. Zhu, Y. Zhu, S. Murali, M.D. Stoller, R.S. Ruoff, ACS Nano 5 (2011) 3333–3338.
[18] L.S. Zhang, L.Y. Jiang, H.J. Yan, W.D. Wang, W. Wang, W.G. Song, Y.G. Guo, J. Mater. Chem. 20 (2010) 5462–5467.
[19] G. Zhou, D.W. Wang, F. Li, L. Zhang, N. Li, Z.S. Wu, L. Wen, G. Qing (Max) Lu, H.M. Cheng, Chem. Mater. 22 (2010) 5306–5313.
[20] Y. Sun, X. Hu, Jimmy C. Yu, Q. Li, W. Luo, L. Yuan, W. Zhang, Y. Huang, Energy Environ. Sci. 4 (2011) 2870–2877.
[21] Y. Shi, B. Guo, Serena A. Corr, Q. Shi, Y.S. Hu, K.R. Heier, L. Chen, R. Seshadri, G.D. Stucky, Nano Lett. 9 (2009) 4215–4220.
[22] Q. Gao, L. Yang, X. Lu, J. Mao, Y. Zhang, Y. Wu, Y. Tang, J. Mater. Chem. 20 (2010) 2807–2812.
[23] A. Manthiram, C. Tsang, J Electrochem. Soc. 143 (1996) L143–L145.
[24] X. Ji, P. SubRamanya Herle, Y. Rho, L.F. Nazar, Chem. Mater. 19 (2007) 374–383.
[25] L.C. Yang, Q.S. Gao, Y. Tang, Y.P. Wu, R. Holze, J. Power Sources 179 (2008) 357–360.
[26] J.R. Dahn, W.R. McKinnon, Solid State Ionics 23 (1987) l–7.
[27] Yoon S. Jung, S. Lee, D. Ahn, Anne C. Dillon, S.H. Lee, J. Power Sources 188 (2009) 286–291.
[28] L.C. Yang, Q.S. Gao, Y.H. Zhang, Y. Tang, Y.P. W, Electrochem. Commun. 10 (2008) 118–122.
[29] Y. Sun, X. Hu, W. Luo, Y. Huang, ACS Nano 5 (2011) 7100–7107.
[30] D.C. Marcano, D.V. Kosynkin, Jacob M. Berlin, A. Sinitskii, Z. Sun, A. Slesarev, Lawrence B. Alemany, W. Lu, James M. Tour, ACS Nano 4 (2010) 4806–4814.
[31] W.S. Hummers, R.E. Offeman, J. Am. Chem. Soc. 80 (1958) 1339.
[32] S.J. Chae, F. Güneş, K.K. Kim, E.S. Kim, G.H. Han, S.M. Kim, H.J. Shin, S.M. Yoon, J.Y. Choi, M.H. Park, C.W. Yang, D. Pribat, Y.H. Lee, Adv. Mater. Mater. 21 (2009) 2328–2333.
[33] H. Kim, Ahmed A. Abdala, Christopher W. Macosko, Macromolecules 43 (2010) 6515–6530.
[34] B. Guo, X. Fang, B. Li, Y. Shi, C. Ouyang, Y.S. Hu, Z. Wang, G.D. Stucky, L. Chen, Chem. Mater. (2011) doi:10.1021/cm202459r.